ACS OMEGA

Open Access

http://pubs.acs.org/journal/acsodf

Article

A 0D Ge(II)-Halide-Based Perovskite with Enhanced Semiconducting Behavior for Electronic Capacitors

Emna Ben Messaoud, Dhouha Abid, Slim Elleuch, Abderrazek Oueslati, Philippe Guionneau, Stanislav Pechev, Nathalie Daro, and Zakaria Elaoud*

Cite This: *ACS Omega* 2024, 9, 42868−42882

Read Online

ACCESS | Metrics & More | Article Recommendations | Supporting Information

ABSTRACT: Perovskite materials have surged to the forefront of materials science, captivating researchers worldwide with their distinctive crystal lattice arrangement and remarkable optical, electric and dielectric attributes. The current study focuses on the development of a novel zero-dimensional (0D) Ge(II)-based hybrid perovskite, formulated as $NH_3(CH_2)_2NH_3GeF_6$, and synthesized through a gradual evaporation process conducted at room temperature. The crystal structure is characterized by an arrangement of organic cations and isolated octahedral $[GeF_6]^{2-}$ groups. This configuration is stabilized by relatively weak intermolecular bonds. A comprehensive analysis of the material's thermal properties using differential scanning calorimetry (DSC) revealed a distinct phase transition occurring at approximately 323 K, which was further confirmed through electrical measurements. The studied compound provided a broad absorption range across the visible spectrum and an optical band gap of 3.30 eV, indicating its potential for semiconducting applications in optoelectronic devices. Photoluminescence PL analysis displays a blueish broad-band emission with a high color rendering index CRI value of 91, when excited at 325 nm. This emission primarily originates from the self-trapped excitons (STEs) recombination in the inorganic $[GeF_6]^{2-}$. Herein, the temperature-dependent behavior of grain conductivity exhibited an Arrhenius-type pattern, with an activation energy (E_a) of 0.46 eV, confirming the semiconductor nature of the investigated compound. In addition, a deep investigation of the alternating current conductivity, analyzed using Jonscher's law, demonstrates that the conduction mechanism is effectively described by the correlated barrier hopping (CBH) model. The dielectric performances show a significant dielectric constant ($\varepsilon' \sim 10^3$). Thus, all these interesting physical properties of this hybrid perovskite have paved the way for advancements in various technological applications, particularly in the field of electronic capacitors.

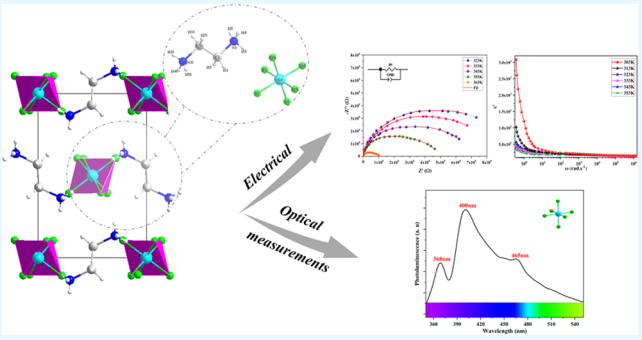

1. INTRODUCTION

Electronic capacitors have recently appeared as one of the most crucial technologies that have significantly improved our daily existence. These components play a pivotal role in the precise control of electric currents and the storage of electrical energy. Their significance lies in their ability to regulate the flow of electricity and store this energy for various applications. These advancements can be found in a wide variety of electronic devices, encompassing smartphones, laptops, appliances, and even electric vehicles.[1−8]

Semiconducting materials, including ceramic, perovskite, porous Metal−Organic frameworks (MOFs), and organometallic materials, have garnered significant progress in the field of electronics as resistors and capacitors.[9−17] Owing to their exceptional physical properties, such as tenability, high electron mobility, low thermal conductivity, better performance, and lower cost of production, hybrid organic−inorganic perovskite materials, with the general formula AMX_3 (where A is the organic cation, M is a metal (Si^{2+}, Sn^{2+}, Ge^{2+}, Pb^{2+}, etc.) and X is a halide anion (Cl^-, Br^-, F^-, etc.)), have particularly demonstrated numerous technological applications. Since these hybrid compounds are made up of inorganic entities and organic cations, inherent properties in both organic and inorganic components are likely to be obtained.[18−23] The outcome of both components' combination offers the opportunity to integrate useful properties inside a single composite, thus giving rise to a broad area of multifunctional materials.[24−26] A hallmark of perovskites lies in their crystal structure, recognized as the perovskite structure, which can be customized across a spectrum of dimensions, spanning from three-dimensional (3D) to zero-dimensional (0D).[27] These crystalline materials are remarkable not only for their superior electrical properties but also for their impressive optical

Received: June 4, 2024
Revised: August 29, 2024
Accepted: September 27, 2024
Published: October 10, 2024

characteristics. This dual functionality renders them highly adaptable to various advanced technologies, from boosting solar energy conversion efficiency to driving innovations in optoelectronic devices.[28] With ongoing research enhancing their performance and stability, perovskites are set to be key players in the future of renewable energy and high-performance electronics.

In particular, the hybrid perovskite $(CH_3NH_3)PbI_3$ compound, is notably appealing owing to its distinctive 3D structure and outstanding optoelectronic characteristics. This compound with a gap band of 1.51 eV, was introduced as a novel material for solar cells, showing promising light absorption and charge transport properties.[29] Another example is the layered two-dimensional (2D) perovskite $(C_6H_5C_2H_4NH_3)_2GeI_4$ which garnered growing interest because of its distinct photophysical attributes and remarkable stability, interesting semiconducting properties with an optical gap energy of 2.12 eV, making it an excellent candidate for photovoltaic applications.[30] Additionally, Chouaib and coworkers synthesized a layered 2D perovskite with the general formula $(C_7H_{10}NO)_2SnBr_6{\cdot}2H_2O$, which demonstrated a good ionic conductivity with an activation energy of Ea_1 = 0.117 eV and Ea_2 = 0.074 eV at 300 K.[31] Similarly, Karoui and colleagues reported a halide-based perovskite-like material namely β-$NH_3(CH_2)_2NH_3SnCl_6$[32] From a structural point of view, the crystal structure of this material is composed of a layered arrangement of distorted $[SnCl_6]^{2-}$ anions and organic $[C_2H_{10}N_2]^{2+}$ groups. Also, Braiek and coauthors reported a new semiconductor perovskite material $(C_5H_6N_2Cl)_2\ SiF_6$, that demonstrated good photophysical properties for electronic devices.[33]

In addition, extensive research efforts have been dedicated to the crystal structure investigation and dielectric characterization of hybrid perovskite compounds such as $NH_3(CH_2)_2NH_3SiF_6$,[34] $NH_3(CH_2)_nNH_3SiF_6$ (n = 2, 3, 4),[35,36] $NH_3(CH_2)_nNH_3SnCl_6$[37,38] and $NH_3(CH_2)_nNH_3MX_6$ (Mn, Co, Tl, Cd···).[39−41] Most of these semiconducting compounds exhibit phase transitions, caused by the reorientation movement of the ammonium cations as well as the movement of H^+ ions through intermolecular hydrogen bonds. Such type of phase transition is known as "order-disorder".

Besides, dielectric relaxation and alternative AC conductivity measurements have been frequently used to better understand the molecular dynamics and the conduction processes of these materials.

As an extension of these previous researches, we report a novel perovskite named ethylenediammonium hexafluorogermannate(II) with the formula $NH_3(CH_2)_2NH_3GeF_6$, which demonstrates impressive electrical and dielectric properties. Its structure presents a zero-dimensional inorganic framework built from the $[GeF_6]^{2-}$ octahedron and organic cations $[NH_3(CH_2)_2NH_3]^{2+}$. The thermogravimetric and Differential Scanning Calorimetry (TGA/DSC) analyses were performed and a phase transition was observed. These studies are supported by a detailed investigation of the semiconducting properties, electric and dielectric mechanisms to understand the origin of the phase transition and extend these results toward the production of efficient and sustainable electronic and optoelectronic devices.

2. EXPERIMENTAL DETAILS

2.1. Raw Materials. Chemical reagents were purchased from a commercial source (Sigma-Aldrich) and used as received without further purification. All these chemical characteristics and the purity of the products used for the preparation of the single crystals of $NH_3(CH_2)_2NH_3GeF_6$ are grouped in Table S1.

2.2. Synthetic Approaches of the $NH_3(CH_2)_2NH_3GeF_6$ Compound. Using the slow evaporation method at room temperature, the preparation of the title compound $NH_3(CH_2)_2NH_3GeF_6$ was carried out in our laboratory from a mixture of ethylenediamine solution with germanium oxide GeO_2 in a molar ratio of 1:1. Hydrofluoric acid was added dropwise in stoichiometric proportions of the mixed solution and then agitated thoroughly for over 15 min. The resulting solution has remained at room temperature for a few days. After recrystallization in an aqueous solution, colorless parallelepipedal crystals suitable for single-crystal X-ray investigation were recovered (Figure S1). The reaction mechanism is given in the following equation

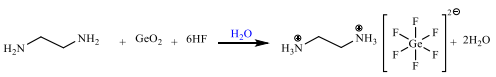

(1)

2.3. Single Crystal X-ray Data Collection. To have a good resolution of the structure of $NH_3(CH_2)_2NH_3GeF_6$ compound, an appropriate transparent crystal of parallelepiped form with dimensions of (0.40 × 0.20 × 0.10) mm^3 was carefully selected at room temperature (293 K) for data collection. Using a Bruker Kappa APEX- II diffractometer and molybdenum radiation ($\lambda_{MoK\alpha}$ = 0.71073 Å), diffracted intensities were gathered within an angular range of $3.8° \leq \theta \leq 32.1°$ resulting in the Miller indices: $-8 \leq h \leq 8$; $-14 \leq k \leq 14$ and $-9 \leq l \leq 9$. This selection allowed the collection of 1305 independent reflections, among which 1144 verify the intensity condition $I > 2\sigma(I)$. Subsequently, the circumstances of the collection, as well as the main results of the refinement relative to the structure of the analyzed compound, are performed using the WinGX platform.[42]

The crystal structural was solved in the monoclinic system, with the centrosymmetric space group $P2_1/n$ and the lattice parameters: a = 5.864(4) Å; b = 9.699(2) Å; c = 6.546(1) Å; and β = 90.184(4)° with two formula units per cell (Z = 2). W80 atoms, including germanium and fluorine, were located using the Patterson method, through the SHELXS-97 program.[43] Additionally, subsequent refinements based on Fourier difference F^2 syntheses have enabled the identification of carbon and nitrogen atoms using SHELXL-2018 program.[44] All these atoms have been anisotropically refined, whereas, the positions of the H atoms were fixed geometrically via the HFIX option. The last refining cycle resulted in satisfying reliability factors of R_1 = 0.048 and wR_2 = 0.147. Figures were drawn by the graphics DIAMOND application.[45]

Crystallographic details related to crystal data collection and structural improvement of the Ge(II)-based perovskite single compound are summarized in Table S2. Atomic positional parameters and anisotropic thermal factors (U_{eq}/U_{iso}) are gathered in the Supporting Information file Tables S3 and S4. Selected bond lengths and angles are reported in Table S5.

2.4. Thermal-Properties Characterization. In order to study the thermal stability of the Ge(II)-based compound, under an oxygen atmosphere, the thermogravimetric measurements (TGA) were gathered on a powdered sample of 2.351 mg in the temperature ranges 303−773 K with a constant heating rate of 10 K/min.

https://doi.org/10.1021/acsomega.4c05255
ACS Omega 2024, 9, 42868−42882

Differential Scanning Calorimetry (DSC) measurement was performed on a 5.800 mg sample with a "DSC 822P METTLER TOLEDO" type device in the temperature range of 243−623 K, at a heating rate of 10 K/min.

2.5. Optical Characterizations. The optical absorption analysis of the $NH_3(CH_2)2NH_3GeF_6$ was carried out on a spin-coated thin film under ambient conditions using a conventional ultraviolet−visible (UV−vis) spectrophotometer (HITACHI, U3300).

The PL spectra were collected using a JOBIN YVON HR 320 spectrophotometer at room temperature under different excitation wavelengths from 280 to 350 nm.

II.VI. Electrical Measurements. The electrical analysis of the Ge-(II)-based halide material was taken with a "1260 Solartron Impedance Analyzer automatic bridge" in the temperature ranging from 303 to 363 K and the frequency range of 10 Hz−7 MHz at an AC voltage of 1 V. To guarantee electrical connections, the polycrystalline sample was pressed employing two silver electrode configurations into a 1.1 mm thickness pellet with an 8 mm diameter.

3. RESULTS AND DISCUSSION

3.1. Insight into the Crystal Edifice. The Single Crystal X-ray investigation reveals that the $NH_3(CH_2)_2NH_3GeF_6$ perovskite compound crystallizes in the monoclinic system with the centrosymmetric space group $P2_1/n$ (C_{2h}), revealing a low dimensional 0D architecture. The formula unit presented in this studied compound is built up of an independent organic cation $[NH_3(CH_2)_2NH_3]^{2+}$ and an isolated octahedral $[GeF_6]^{2-}$ anion. It is to be noticed that the germanium atom occupies a special position with a Wyckoff site of 2a, while all other atoms occupy general positions (Wyckoff sites 4e). The formula unit of this compound is depicted in Figure 1.

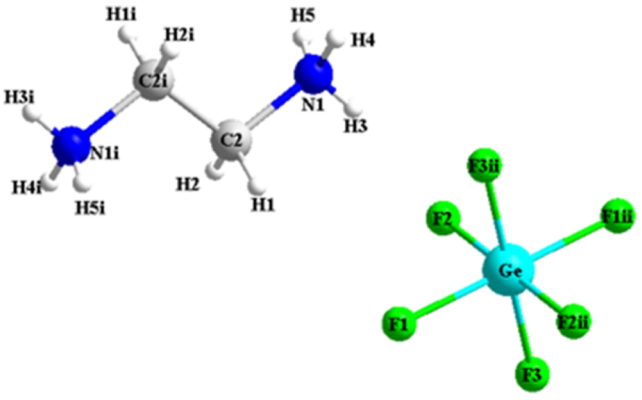

Figure 1. Formula unit of the Ge-based perovskite compound.

Figure 2a,b depicts the arrangement of the crystal structure along the *ab* and *bc* planes. The examination of the structure reveals a pseudolayered arrangement of $[GeF_6]^{2-}$ isolated octahedrons within the crystal structure, alternated with organic $[NH_3(CH_2)_2NH_3]^{2+}$ cations. It also revealed that these entities are interconnected through a network of hydrogen bonds, resulting in a three-dimensional network.

Within the inorganic $[GeF_6]^{2-}$ groups, each Ge (II) atom is surrounded by six fluorine atoms F_1, F_2, F_3, F_{1ii}, F_{2ii}, and F_{3ii} (where; (ii): x, $-z$, $-y$), conferring a slightly distorted octahedral geometry. A close look at Figure 2a,b shows that these isolated inorganic octahedrons are placed at $x = 0$ and $z = 0$ as well as in the center of the unit cell. As quoted in Table S5 and Figure 2c, the average values of Ge−F interatomic distances vary between 1.762(3) and 1.776(3) Å, and the F−Ge−F angles fall in the range of 88.95(15)−180.00(16)°. All these geometric characteristics are in good agreement with the similarities of those found in previously reported compounds like $NH_3(CH_2)_2NH_3SiF_6$, $NH_3(CH_2)_3NH_3SiF_6$[34,35] and $\langle\beta\rangle NH_3(CH_2)_2NH_3SnCl_6$.[32] Therefore, considering the geometrical characteristics of the $[GeF_6]^{2-}$ octahedral, the average of the distortion indices (ID) are calculated using the distortion equation indices of Baur:[46]

$$ID_{d(Ge-F)} = \sum_{i=1}^{i=6} \frac{d_i - d_m}{6d_m} \quad (2)$$

$$ID_{a(F-Ge-F)} = \sum_{i=1}^{i=15} \frac{a_i - a_m}{15a_m} \quad (3)$$

where; d_m/a_m represents the values of the average distances/angles of the metal−ligand bonds (Ge−F) and d_i/a_i denotes the values of the distances/angles of the metal−ligand bonds (Ge−F). These calculated values were: $ID_{d\ (Ge-F)}$ = $4.7107.10^{-4}$ and $ID_{a\ (F-Ge-F)}$ = 0.01854. Lower distortion indices suggest that the metal's coordination geometry is a slightly deformed octahedron.

In the case of the organic groups, the diprotonated ethylenediammonium cations exhibit a trans-configuration. These latter are placed in the middle of the edges. Thus, the C2−C2i and C2−N1 bond distances are respectively 1.516(9) and 1.493(6) Å, however, the N1−C2−C2i angles are of the order of 109.2(4)° (symmetry codes, ((i): $-x$, $-y+1$, $-z$)) (Table S5). These average values are similar to those observed in other $[NH_3(CH_2)_2NH_3]^{2+}$ based compounds, like $[NH_3(CH_2)_2NH_3]SnCl_6$,[32] $[NH_3(CH_2)_2NH_3]Cd(SCN)_4$[47] and $[NH_3(CH_2)_2NH_3]CdCl_4$.[41]

In addition to the above, the study of the crystal packing of the Ge(II)-based halide perovskite reveals that the polymeric network is stabilized through intermolecular hydrogen bonds N−H···F et C−H···F as well as van der Waals interactions. As shown in Figure 3a, the octahedron $[GeF_6]^{2-}$ is coordinated by four centrosymmetric organic $[C_2H_{10}N_2]^{2+}$ entities. Indeed, the N−H···F bonds vary from 3.112(5) to 2.897(5) Å and the angles between 134(6) to 171°(5). Whereas, the C−H···F bonds are comprised between 3.236(5) and 3.340(5) Å, and the angles range from 132(4) to 136(4)°. All These selected hydrogen bond distances and angles are summarized in Table S6. As per the findings of Brown's research,[48] hydrogen bonds are considered weak if the distance between a donor atom and an acceptor fluorine atom exceeds 3.19 Å. In this context, the C−H···F bonds to fluorine ($d_{C2-H1\cdots F2iii}$ = 3.236 Å and $d_{C2-H2\cdots F1iv}$ = 3.340 Å) are considered as weak bonds, while the bonds of the N−H···F intermolecular interaction involving is regarded as strong with $d_{D\cdots A}$ < 3.19 Å. Consequently, these various intermolecular interactions give birth to a 3-D framework (Figure 3b).

3.2. Thermal TGA-DSC Analysis. The thermal behavior of the perovskite $NH_3(CH_2)_2NH_3GeF_6$ compound was studied by the simultaneous (dTG-TGA)-DSC experiments, in the range of 243−750 K. The results are presented in Figure 4. The TGA profile reveals an initial weight loss occurring between 300 and 367 K (mainly at 310 K according to the dTG curve) corresponding to 2.8% mass loss which is assigned to the removal of adsorbed water molecules due to the

https://doi.org/10.1021/acsomega.4c05255
ACS Omega 2024, 9, 42868−42882

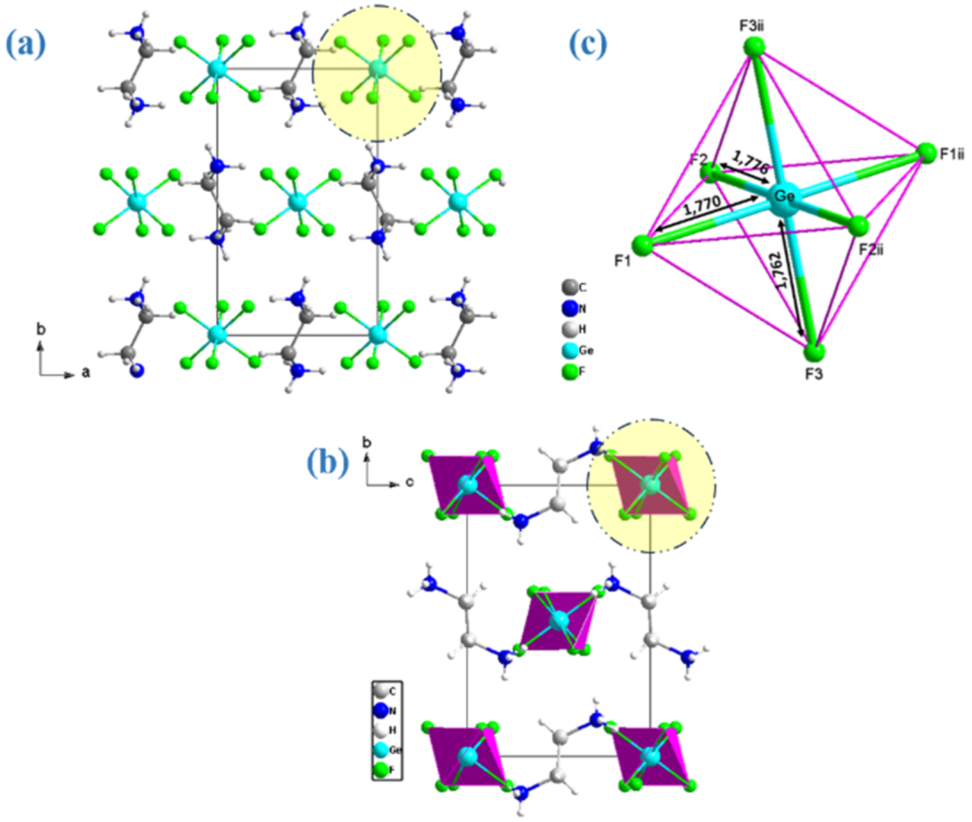

Figure 2. Atomic arrangement of the organic and inorganic along the (a) *ab* and (b) *bc* planes. (c) Geometric description of the inorganic framework $[GeF_6]^{2-}$.

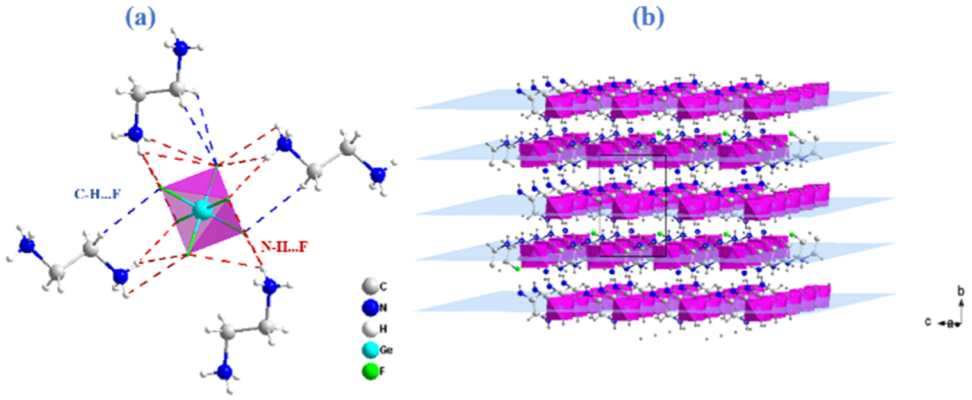

Figure 3. (a) Scheme of hydrogen-bonding interactions. (b) Perspective view of the $[NH_3(CH_2)_2NH_3]GeF_6$ compound.

sample's hygroscopic nature. Such a phenomenon is observed for several compounds, particularly $[(R)\text{-}C_9H_{14}N]_3[CuBr_4]$. Br hybrid material.[49] The second whole mass loss observed between 393 to 773 K with 84.67% (calc.: 86.08%) loss of the total weight is associated with the decomposition of the polymeric network, resulting in the formation of GeO_2 as the final residue. The DSC thermogram displays an endothermic peak located at 321.71 K. Indeed, this endothermic behavior can be linked to a phase transition. The characteristic dynamical values of this transition are ΔH_1 = 1216.93 J mol^{-1} and ΔS_1 = 3.782 J $mol^{-1}K^{-1}$. Thus, two sequential endothermic peaks pointed at 584 and 609.53 K are linked with the fusion followed by subsequent decomposition of the title compound. The average variations of enthalpy and entropy of these two peaks are ΔH_2 = 5377.11 × 10^2, ΔH_3 = 44051.73 J mol^{-1}, and ΔS_2 = 920.72 J mol^{-1} K^{-1}, respectively. Upon cooling, the irreversibility of this material indicates the decomposition process.

3.3. Optical Properties. *3.3.1. UV−Visible Study.* To thoroughly comprehend the semiconducting properties of the $(NH_3(CH_2)_2NH_3)$ GeF_6 compound, we conducted experimental UV−visible absorption spectroscopy at room temperature. The measurements spanned the spectral range of 250−600 nm, providing detailed insights into the compound's optical behavior (Figure 5a). It is widely understood that the optical characteristics of the $[ns^2(n-1)d^{10}np^2]$ organic−inorganic materials mainly result from the electronic transitions of inorganic anions.[50,51] In the ultraviolet range, a strong Gaussian-shaped absorption band around 342 nm with high energy (3.62 eV), is observed and assigned typically to the

https://doi.org/10.1021/acsomega.4c05255
ACS Omega 2024, 9, 42868−42882

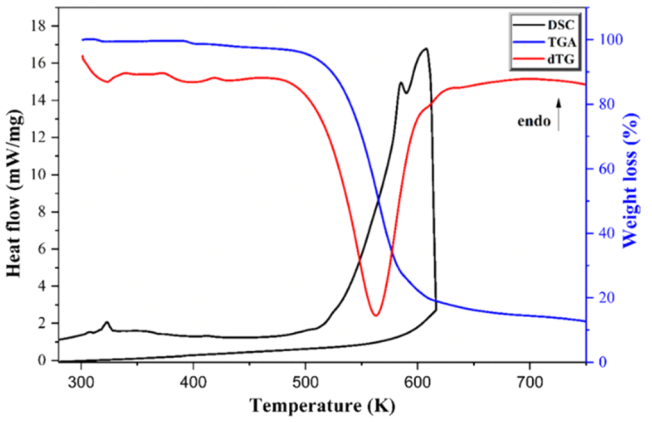

Figure 4. (TGA-dTG)-DSC curves of the $[NH_3(CH_2)_2NH_3]GeF_6$ at 10 K/min.

excitation of free electron−hole pairs confined within the inorganic $[GeF_6]^{2-}$ octahedron, where an electron is stimulated from the valence band to the conduction band during excitation, establishing a hole in the valence band.[24,32] On the other hand, a peak followed by a shoulder bond at (2.99 eV) at 414 nm might be assigned to the ligand-to-metal charge transfer (LMCT) excited state.

The optical gap energies between the conduction and valence bands of the Ge(II)- based hybrid compound were estimated by the Tauc relation:[52]

$$\alpha h\nu = A(h\nu - E_g)^n \tag{4}$$

where A is a constant, E_g is the optical band gap and n is a constant that determines the type of optical transitions (n = 1:2 for the direct transition and n = 2 for the indirect transition).

The optical absorption coefficient α is determined using the Beer−Lambert relationship:

$$\alpha = \frac{2.303 \times \mathrm{Abs}}{d} \tag{5}$$

where d and Abs are the layer thickness and the absorbance, respectively.

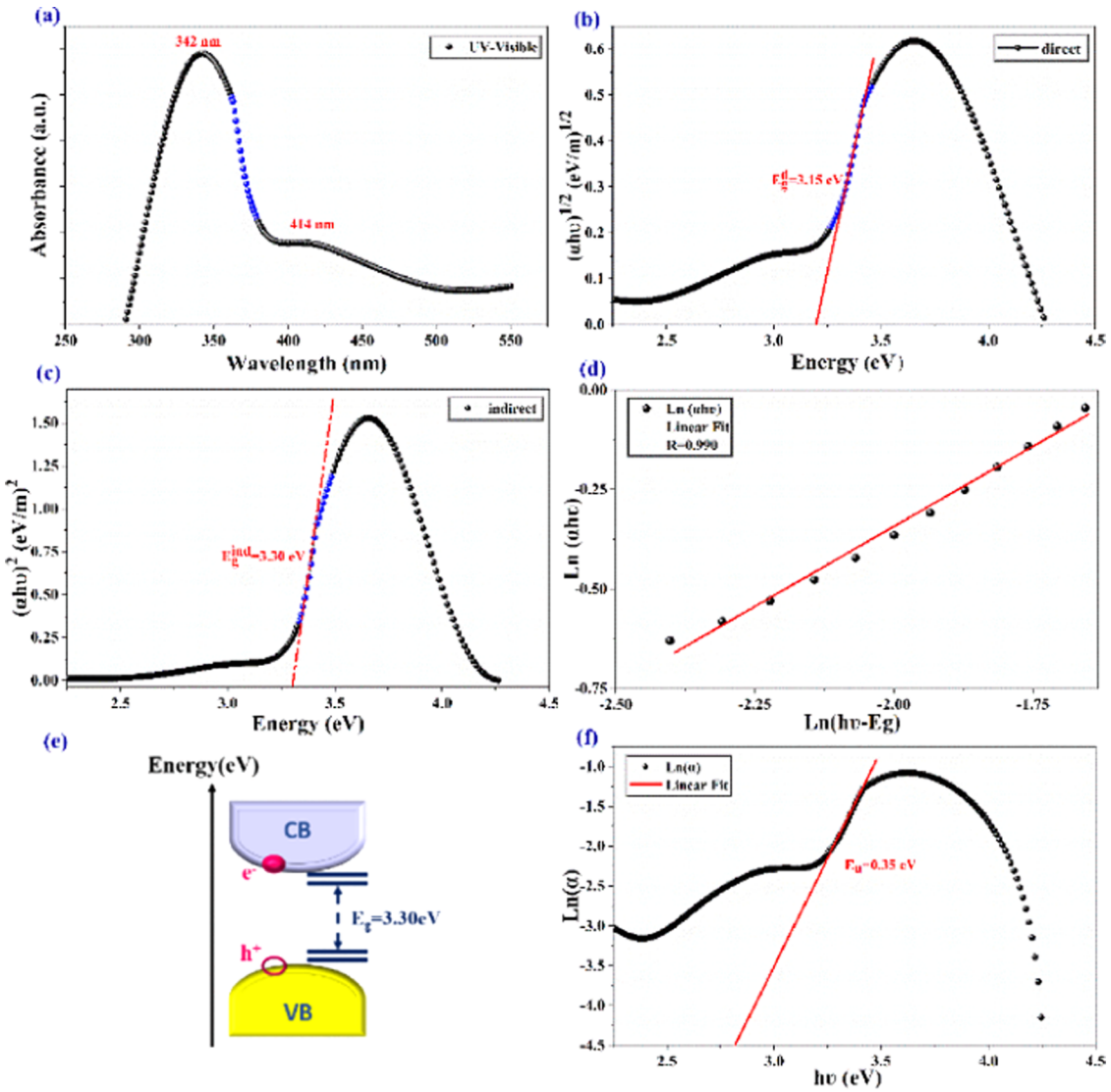

Figure 5. (a) Normalized absorption spectrum. (b, c) Plots of (b) $(\alpha h\nu)^{1/2}$ and (c) $(\alpha h\nu)^2$ versus $(h\nu)$. (d) Dependence of $\ln(h\nu - E_{op})$ as a function of $\ln(Ah\nu)$. (e) Gap energy between CB and VB. (f) Variation of $\ln(\alpha)$ as a function of $(h\nu)$ for the Ge-based title compound.

https://doi.org/10.1021/acsomega.4c05255
ACS Omega 2024, 9, 42868−42882

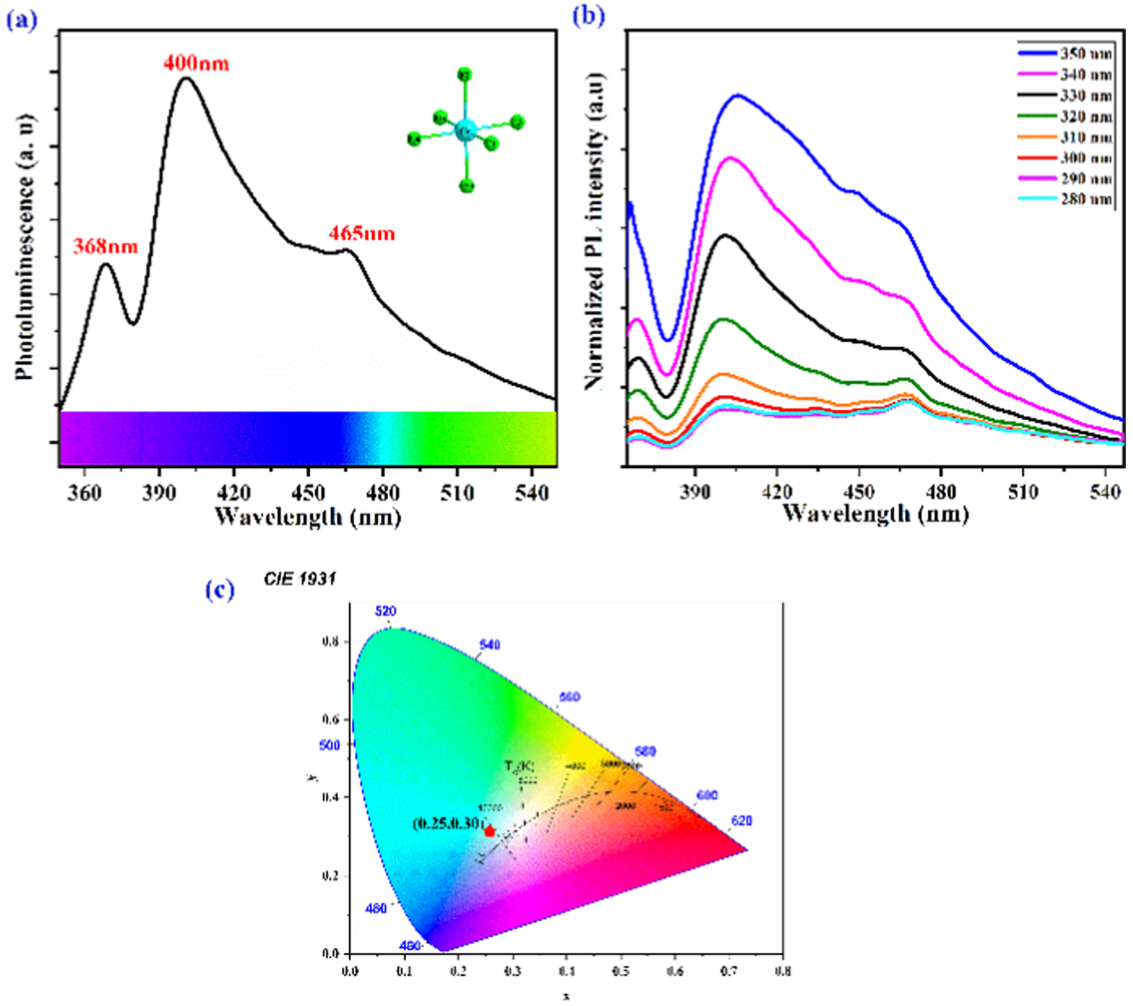

Figure 6. (a) Slide-state photoluminescence spectrum at 325 nm. (b) Normalized PL emission spectra of the title compound excited from 280 to 350 nm. (c) CIE chromaticity coordinates of the Ge-halide crystals during the PL analysis.

The dependence of $(\alpha h\nu)^{1/2}$ and $(\alpha h\nu)^2$ on the photon energy is shown in Figure 5b,c for the $NH_3(CH_2)_2NH_3$ GeF_6 compound. Through a slight fitting of the Tauc plots (Figure 5d), the direct and indirect band gap energies were found to be E_g^d = 3.15 eV and E_g^{in} = 3.30 eV, respectively. The optical band gap energies were determined according to the following formula:

$$n = \ln(\alpha h\nu)/\ln[A(h\nu - E_g)] \quad (6)$$

In inset Figure 5d,e, the optical gap energy $E_g(op)$ was inferred by extending the linear region of the curve to intersect the *x*-axis. A direct permitted transition is confirmed by the slope on this plot, which produces a value of n equal to 0.802, confirming an indirect gap transition (3.30 eV). In this matter, the obtained energy gap value is superior compared to other hybrid organic−inorganic Ge-based compounds, such as $(C_6H_5C_2H_4NH_3)_2GeI_4$ (2.12 eV)[30] and $(CH_3)_3NH$ GeI_3 (2.8 eV).[53] Assessing these outcomes, the $NH_3(CH_2)_2NH_3GeF_6$ material is qualified as a wide band gap semiconductor. This classification opens up a range of advanced applications, particularly in the fabrication of Light light-emitting diodes (LEDs) and photodetectors.[54,55]

The Urbach energy (E_u) is a parameter that describes the exponential tail of the absorption spectrum near the bandgap energy in semiconductors. It is associated with disorders and defects in the material, offering insights into the quality and crystallinity of the semiconductor.[56] The following equation provides the value of E_u:

$$\ln(\alpha) = \ln(\alpha_o) + (h\nu/E_u) \quad (7)$$

where α_0 is a constant, E_u represents the Urbach energy (eV) and $(h\nu)$ is the photon energy (eV).

The $\ln(\alpha)$ as a function of $(h\nu)$ is illustrated in Figure 5f. The inverse of the slope of the linear part leads to the calculated value E_u which is equal to 0.35 eV, presenting only 10% of the band gap energy. This result suggests a tighter distribution of localized states in the band gap, indicating lesser disorder, fewer flaws, and imperfections in the structure of the investigated Ge-based perovskite.[57,58]

The Urbach energy may be more effectively utilized by employing the following expression:

$$E_u = \frac{k_B \times T}{\beta(T)} \quad (8)$$

where k_B is the Boltzmann's constant, T is the ambient temperature and the term $\beta(T)$ refers to the steepness of a material's absorption edge caused by electron−phonon interactions inside the band gap.[59] This latter parameter, with the value of 0.073, is linked to the force of the electron−phonon interaction (E_{e-ph}) according to the expression

https://doi.org/10.1021/acsomega.4c05255
ACS Omega 2024, 9, 42868−42882

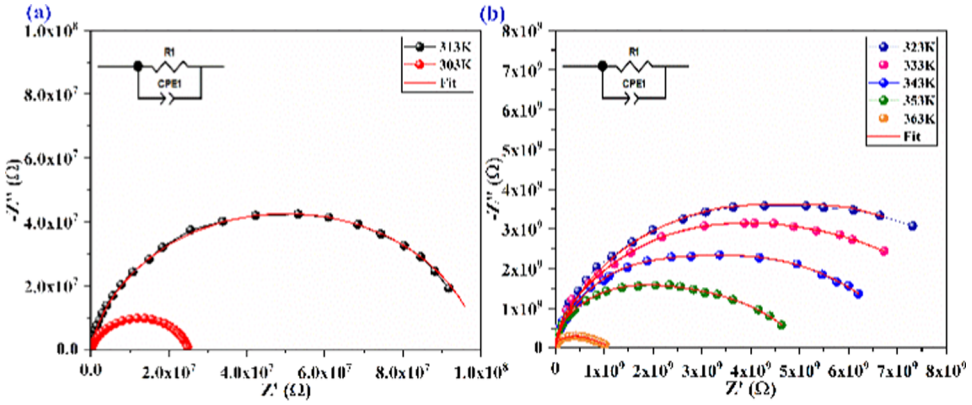

Figure 7. Variation of the Nyquist plots measured at different temperatures (a) 303−313 K and (b) 323−363 K with the proposed equivalent circuits for the investigated compound.

$$E_{e-ph} = \frac{2}{3 \times \beta(T)} \quad (9)$$

The predicted electron−phonon interaction strength (E_{e-ph}) is around 15.5 eV.

3.4. Photoluminescence Properties Analysis. The photoluminescence properties of the Ge(II)-based compound were measured under 325 nm UV excitation at room temperature (Figure 6a). According to this figure, three distinct bluish emission peaks are observed: two peaks observed at 368 nm (3.37 eV) and 400 nm (3.10 eV), and a weak band emission at 465 nm (2.66 eV).

The first medium band at 368 nm is allocated to the electronic transition ligand−metal. However, the two-emission bands around 400 and 465 nm, are attributed, respectively, to the excitons localized within the inorganic $(GeF_6)^{2-}$ octahedrons, caused by self-trapped excitonic states resulting from the distortion of the inorganic groups. It was recently demonstrated that the formation of self-trapped excited (STEs) states in organic−inorganic hybrids is well recognized to be dependent on the crystalline system's dimensionality, with lower dimensionality (0D).[60−63] In this matter, the blue broadband emission of the Ge-based perovskite is caused by the recombination of STEs, due to the inorganic anions. For a deep comprehension of the emission phenomenon, we have examined the normalized PLE spectra at various excitation wavelengths from 280 to 350 nm (Figure 6b). It is evident to notice that the Stokes shift decreases remarkably with increasing excitation and emission wavelength values. According to Figure 6b, the largest Stokes shift value of 121 nm (1.347 eV) was observed under excitation at 280 nm (4.437 eV). This phenomenon is commonly ascribed to self-trapped excitons (STEs), which are induced by powerful exciton−phonon interactions in low-dimensional (0D) systems. Such interactions produce a wide 400 nm emission band, followed by the medium−sharped peak at 465 nm.

As asserted in Figure 6c, based on the chromaticity diagram (CIE 1931), the investigated material exhibits a CIE_x, CIE_y coordinates of (0.25; 0.30) upon excitation at 325 nm, lying inside the range of bluish light's color spectrum. Besides, the broad-band emission from this material reveals a Correlated Color Temperature (CCT) value of 10,982 K, which falls into the category of "cold" blue light. Additionally, the index CRI measures the ability of a light source to reveal the colors of various objects faithfully in comparison with an ideal or natural light source. It is expressed as a number on a scale from 0 to 100, where higher values indicate better color rendering. Here, his novel compound has a CRI of 91, surpassing that of commercial light diodes (CRI = 80) and white light hybrid perovskite.[64] This value is the highest one compared with previously reported halide-based hybrid materials, including $(C_6H_{10}N_2)[SnCl_3]Cl$ (CRI = 92),[63] AEA $PbBr_4$ (CRI = 87),[64] $(C_4H_9NH_3)_2PbCl_4$ (CRI = 86),[62] $(C_4N_2H_{14}Br)_4SnBr_6$ (CRI = 70)[65] and $(C_4N_2H_{14})PbBr_4$ (CRI = 63).[66]

3.5. Electrical Properties. *3.5.1. Impedance Complex Analysis and Equivalent Circuit.* The complex impedance spectroscopic technique attempts to analyze the electrical characteristics of materials in a wide range of frequencies and temperatures. It is extremely useful in determining the contributions of various mechanisms in the conduction process such as grain, grain boundary, and the electrode-material interface impact. Although it does come with certain limitations and complexity that necessitate careful complementary interpretation.

Figure 7 depicts the variation of the Nyquist plots measured from 303 to 363 K, providing knowledge of the resistive (real part Z') and reactive (imaginary part Z'') elements in this synthesized $NH_3(CH_2)_2NH_3GeF_6$ material. These diagrams exhibit some deviations of the Z'-axis, indicating Cole−Cole type behavior. At the low-temperature region (beneath T = 323 K), we observe that as the temperature rises, the radius of the semicircles increases, indicating a decrease in thermal conductivity, as can be seen in Figure 7a. Such behavior is mainly due to the presence of water molecules in the air (humidity), which is confirmed by TGA analysis. These water molecules could be incorporated into the grain boundary pores and behave as a catch center for charge carriers. This phenomenon is commonly observed in organic− inorganic-halide-based materials.[49]

In an area of high temperatures (upper T = 323 K), when the temperature rises, the diameter of the semicircles decreases corresponding to the resistance decreases and increasing conductivity. This is a sign of an active conduction mechanism within the sample of dielectric character (Figure 5b).[67]

The modeling of the various spectra $-Z'' = f(Z')$, using the Z-view software, allowed us to isolate an equivalent circuit composed of two elements coupled in parallel: a gain resistor (R_1) and a fractal capacitor (CPE_1).[17,68] The impedance of the capacity of fractal interface CPE is determined by the following expression:

https://doi.org/10.1021/acsomega.4c05255
ACS Omega 2024, 9, 42868−42882

$$Z_{CPE} = \frac{1}{Q_0(j\omega)^{\propto}} \tag{10}$$

Taking into account the adopted equivalent circuit, the expressions for the real and imaginary parts of the complex impedance are as follows:

$$Z' = \frac{R^2 Q_0 \omega^{\alpha} \cos\left(\frac{\alpha\pi}{2}\right) + R\infty}{\left(1 + RQ_0\omega^{\alpha}\cos\left(\frac{\alpha\pi}{2}\right)\right)^2 + \left(RQ_0\omega^{\alpha}\sin\left(\frac{\alpha\pi}{2}\right)\right)^2} \tag{11}$$

$$Z'' = \frac{R^2 A_0 \sin\left(\frac{\alpha\pi}{2}\right) + R\infty}{\left(1 + RQ_0\omega^{\alpha}\cos\left(\frac{\alpha\pi}{2}\right)\right)^2 + \left(RQ_0\omega^{\alpha}\sin\left(\frac{\alpha\pi}{2}\right)\right)^2} \tag{12}$$

where Q indicates the value of the capacitance of the CPE element, α presents the degree of deviation between the radius of the semicircle and the Z' axis in the Nyquist representation and R is the polarization resistance, which describes the electrical resistance of the material.

We emphasize that the excellent correlation between the experimental and computed results demonstrates that the proposed equivalent circuit, describes the electrical behavior of the synthesized material.[69] The extracted parameters of the equivalent circuit element (R, Q, and α) are symmetrized in Table S7. Upon $T > 323$ K, it is clear that the temperature increases with decreasing the gain resistance (R) as well as a notable change in the constant of the CPE (Q), and the phase angle (α). This decrease in the resistive property indicates the existence of an activated conduction mechanism.

The fluctuation of the real portion of the impedance complex (Z') as a function of frequency and temperature is plotted in Figure S2. We see that the amplitude of Z' is higher in the low-frequency band at low temperatures. Then, when temperature and frequency increase, Z' decreases gradually. Its behavior validates an enhancement in DC conductivity inside the title compound. At high frequencies, all the curves of Z' at all temperatures merge, implying a probable release of space charge and a reduction in barrier characteristics.[70]

Figure S3 illustrates the variation of ($-Z''$) versus frequency at various temperatures. These charts demonstrate that Z'' climbs with increasing temperature and frequency until reaching a maximum Z'' and then progressively falls. In this matter, the peak broadening suggests the occurrence of a relaxation process within the system.[71] Moreover, a merging of all curves is observed as the frequency decreases, suggesting a possible release of the charge carriers. In fact, at high frequencies, the charge carriers have less time to relax, and their polarization diminishes with an increase in frequency, leading to fusion.[72] Further, this discovery reflects a decrease in resistance characteristics.[73]

The variation of the complex impedance (Z' and Z'') versus frequency at 313 K is presented in Figure S4. It is noteworthy that Z'' increases in frequency while Z' drops. This process continues until Z'' attains its maximum (Z''_{max}) and intersects with Z' plot. This highest value is associated with a particular frequency, known as f_p (relaxation frequency). Eventually, as the frequency rises, Z' and Z'' decrease until they reach zero.[74]

The acquired bulk resistance (R_g) values pertaining to the grain at various temperature ranges permitted the determination of the electrical conductivity σ_{dc}, described by the following equation:

$$\sigma_{dc} = \frac{e}{R \times S} \tag{13}$$

where S stands for the surface area, while e corresponds to the thickness of the pellets.

The thermal evolution of this specific conductivity is plotted in Figure 8. According to this figure, two regions are observed

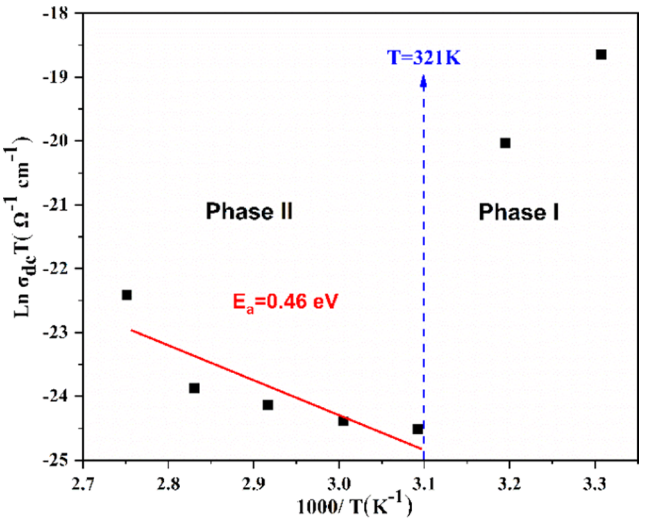

Figure 8. Temperature dependence of the conductivity for the $[NH_3(CH_2)_2NH_3]GeF_6$.

at $T > 323$ K and $T < 323$ K with a noticeable change in the slope around 323 K, confirming the phase transition observed by the DSC study. Besides, at $T > 323$ K, the curve shows a remarkable increase in the electrical conductivity (σ_{dc}) as the temperature increases. These results indicate that the conduction follows a thermally activated transport mechanism, which is dictated by the Arrhenius law:

$$\sigma_{dc}T = \sigma_o \exp(-E_a/kT) \tag{14}$$

where σ_0 is the pre-exponential factor, E_a is the activation energy, k is the Boltzmann constant and T is the absolute temperature. By applying this principle, the gradient of the plot $\log(\sigma T)$ against $10^3/T$ yields an activation energy of $E_a = 0.46$ eV. In the second phase ($T < 323$ K), it is evident that the conductivity deviates from the behavior predicted by the Arrhenius law. This observation supports the hypothesis of water evaporation within this temperature range. This material exhibits a hygroscopic nature, which in turn impacts the fluctuation in conductivity.[75]

3.6. AC Conductivity. To explore how the material responds dynamically to an applied alternating electric field, an analysis of the alternating current conductivity was carried out. The alternating conductivity, denoted as σ_{ac}, is determined through the following equation:

$$\sigma_{ac} = \left(\frac{e}{s}\right) \times \left(\frac{Z'}{Z'^2 + Z''^2}\right) \tag{15}$$

The variation of σ_{ac} versus $\log(f)$ is illustrated in Figure 9a. It is clear that the alternating conductivity σ_{ac} increases with rising frequency and temperature. At low frequencies, a plateau of direct current σ_{ac} is observed due to the frequency-

https://doi.org/10.1021/acsomega.4c05255
ACS Omega 2024, 9, 42868−42882

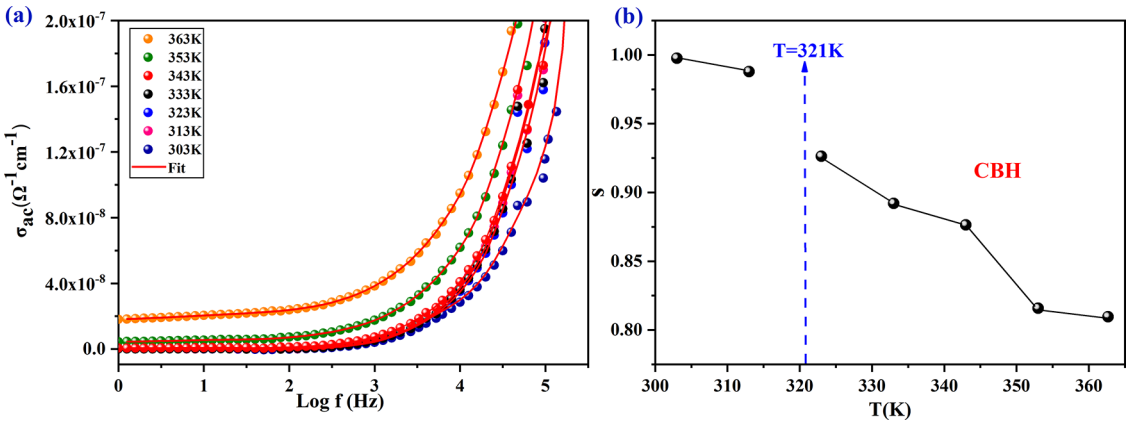

Figure 9. (a) Changes in the alternative AC conductivity versus frequency at various temperatures and (b) plot of the exponent '*s*' versus temperature for the Ge-based perovskite.

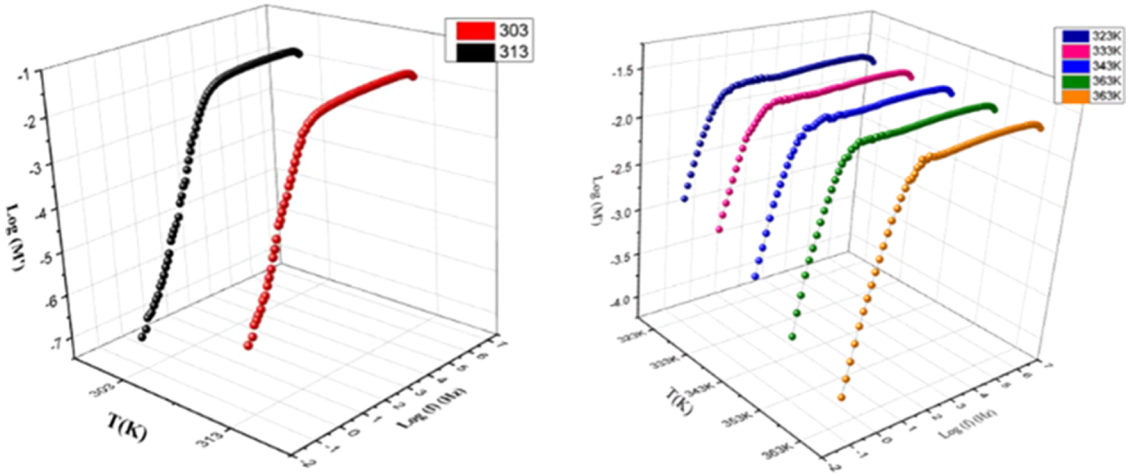

Figure 10. Variation of the real part of the modulus formalism as a function of frequency, at several temperatures for the Ge-halide title compound.

independent conductivity that occurs from the random distribution of charge carriers. The bearing becomes increasingly obvious, indicating that this regime is engaged thermally. Afterward, the $\sigma_{(ac)}$ plots exhibit some dispersion toward high frequencies due to interactions between charge species.[76,77]

The phenomenon of conductivity dispersion (σ_{ac}) can be theoretically described by Jonscher's law as follows:[78]

$$\sigma_{ac} = \sigma_{dc} + A\omega^{s} \tag{16}$$

where σ_{dc} is the DC conductivity, ω is the angular frequency of measurement, A is constant and s is the power law exponent that reflects the degree of interaction between mobile ions and their surroundings, varying between 0 to 1. To determine the predominant conduction mechanism of the AC conductivity in the studied compound, analyzing the variation of the exponent "*s*" as a function of temperature provides valuable insights into these conduction models. Above T = 321 K, the value of '*s*' decreases with rising temperature, suggesting that the Correlated Barrier Hopping (CBH) model governs the electrical transport in this material (Figure 9b). This model applies to different organic−inorganic hybrid materials, such as the $[(CH_3)_2NH_2]_2ZnBr_4$[79] and $(C_6H_9N_2)_2[Sb_2Cl_8]$.[80]

3.7. Modulus Analysis. The utilization of electric modulus formalism proves to be an advantageous metric for obtaining a deeper understanding of both the charge transport mechanism and the relaxation process within the examined compound. However, it may be less effective in resolving contributions from grain boundaries and interfaces.

The M^* formalism is delineated through the following equations:

$$M^* = 1/\varepsilon^* = i\omega C_o Z^* = M' + jM'' \tag{17}$$

$$M' = (\varepsilon')/((\varepsilon'^2 + \varepsilon''^2)) \tag{18}$$

$$M'' = (\varepsilon'')/((\varepsilon'^2 + \varepsilon''^2)) \tag{19}$$

where M', M'': are respectively, the real and imaginary parts of the complex electrical modulus M^*, Z^* presents the complex impedance and C_0 is the vacuum capacitance of the cell, calculated as $C_0 = \varepsilon_0 S/e$, where ε_0 denotes the permittivity of free space, S: the contact area between the electrolyte and electrode, e signifies the thickness of the sample, and ω corresponds to $2\pi f$, with f denotes the frequency in Hertz (Hz).

To validate these contributions, we generated a plot of $\log(M')$ against $\log(f)$ at several temperatures (Figure 10). At low frequencies, the real part of the complex modulus (M') is very low, suggesting minimal influence of the electrodes. This behavior indicates that the electric field is not strong enough to facilitate the long-range movement of the charge carriers. Instead, the conduction process is dominated by the short-

https://doi.org/10.1021/acsomega.4c05255
ACS Omega 2024, 9, 42868−42882

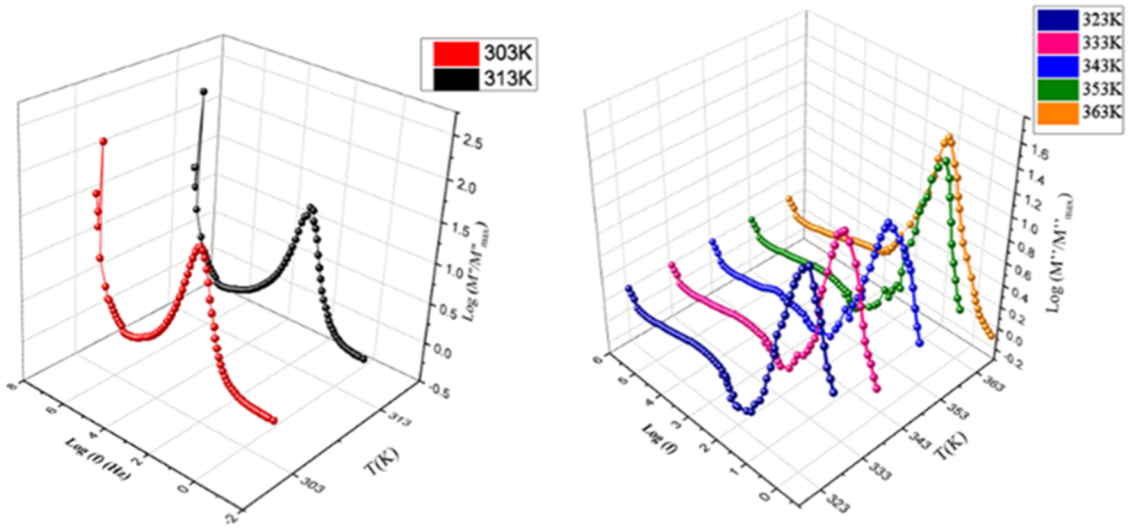

Figure 11. Three-dimensional plot depicting the change in $\log(M''/M''_{max})$ as a function of $\log(f)$ for the $[NH_3(CH_2)_2NH_3]GeF_6$ compound.

range mobility of these carriers. As the frequency increases, M' initially decreases and then gradually rises, eventually approaching a constant value at high frequencies ($M'^{\infty} = 1/\varepsilon'^{\infty}$). This plateau at high frequencies signifies the presence of a relaxation process within the material.[81] The relaxation process is characterized by the ability of the charge carriers to respond to the alternating electric field, indicating their involvement in a localized polarization process rather than contributing to long-range conduction.

Figure 11 displays the three-dimensional representation of the normalized imaginary part of the electrical modulus M''/M''_{max} versus $\log(f)$ at different temperatures for the $NH_3(CH_2)_2NH_3GeF_6$ compound. It is evident that all graphs exhibit a clearly defined relaxation peak, with the maximum shifting toward higher frequencies with rising temperature. This behavior may reflect a transition from short-distance mobility to long-distance mobility of charge carriers. The ions are mobile over large distances in the low-frequency region, whereas they seem to be confined to their potential wells and move over short distances in the high-frequency range located to the right of the maximum peak.[17] These facts reflect a temperature-dependent relaxation process. Each asymmetric peak maximum (M''_{max}) corresponds to a characteristic frequency f_p ($f_p = 1/2\pi\tau_{max}$).[82,83]

In general, the electric relaxation mechanism is well-defined by the Kohlrausch−Williams−Watts (KWW) function:

$$\phi(t) = \exp\left[-\left(\frac{t}{\tau\sigma}\right)^{\beta}\right] \tag{20}$$

where β is the Kohlrausch parameter that characterizes the degree of non-Debye behavior.

Figure 12 suggests the variation of the σ_{dc} and $\log(f_p)$ as a function of $1000/T$ for the title compound. These two graphs show two quasi-parallel lengths with a discontinuity at $T = 323$ K, approving the phase shift found by conductivity and thermal examinations.

3.8. Dielectric Studies. Permittivity analysis is essential for understanding the dielectric properties of materials, including their ability to store and dissipate electrical energy. Its primary advantage lies in providing detailed information about the dielectric constant and dielectric loss, which are crucial for

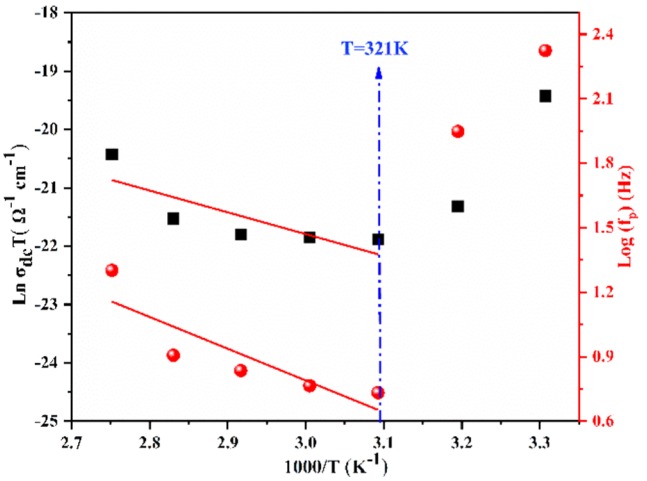

Figure 12. Variations of σ_{dc} and $\log(f_p)$ as a function of $1000/T$ for the title compound.

applications in capacitors and other electronic devices. However, permittivity measurements can be influenced by extrinsic factors such as temperature, humidity, and electrode effects, complicating the interpretation of results and potentially obscuring the material's inherent properties. To confirm the phase transition observed in the DSC and electrical measurements, we carefully examine the variation of the permittivity. The complex dielectric function is expressed mathematically as follows:[84]

$$\varepsilon^* = \varepsilon' + i\varepsilon'' \tag{21}$$

The real and imaginary parts of the electric permittivity were calculated according to the following relations:

$$\varepsilon' = \frac{-Z''}{\omega C_0(Z'^2 + Z''^2)} \tag{22}$$

$$\varepsilon'' = \frac{-Z'}{\omega C_0(Z'^2 + Z''^2)} \tag{23}$$

Figure 13a,b illustrates the temperature dependence of the real and imaginary parts of the dielectric conductivity (ε' and ε'') of the $NH_3(CH_2)_2NH_3GeF_6$ compound at selected

https://doi.org/10.1021/acsomega.4c05255
ACS Omega 2024, 9, 42868−42882

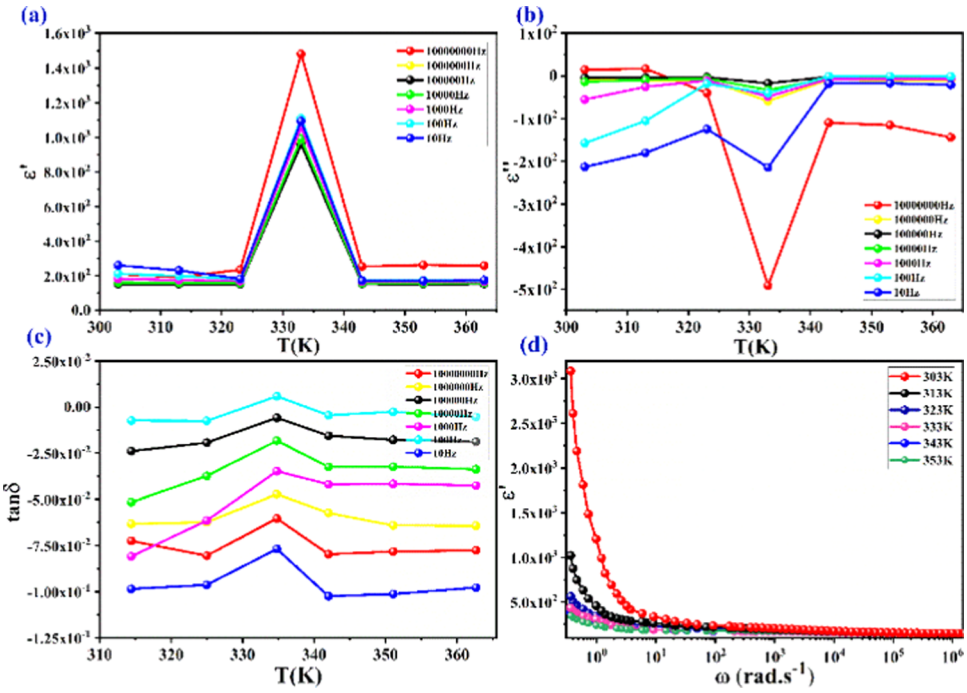

Figure 13. Temperature dependence of (a) the real part (ε') and (b) the imaginary part (ε''). (c) Variation of the dissipation factor ($\tan(\delta)$) with frequency. (d) Frequency dependence of the real part of the permittivity (ε') at different temperatures of $[NH_3(CH_2)_2NH_3]GeF_6$.

frequencies between 10 Hz and 10^7 Hz. An overview of the data gathered reveals the presence of dielectric abnormally around T = 321 K, featuring the detected phase transition already observed in the thermal and electrical analyses. Below 320 K, the variation of ε' and ε'' reaches a constant value with increasing frequency. This phenomenon arises due to the limited reorientation movements of the charge carriers, preventing them from aligning themselves with the direction of the applied electric field.

Henceforth, above T > 320 K, the dielectric permittivity ε' shows a maximum in the real part curves and a minimum in the ε'' plots at T = 331 K, align with the temperature observed at DSC curves (T = 321.5K) and then decreases progressively. Such behavior is in agreement with the occurrence of a conductivity relaxation within this synthesized compound.[85]

The dielectric loss factor ($\tan\delta$) was computed using the following equation:

$$\tan\delta = \frac{\varepsilon''}{\varepsilon'} = \frac{1}{2\pi RC} \quad (24)$$

where ε' and ε'' are the real and imaginary components of the dielectric constant, respectively. C and R represent the capacitance and resistance of the sample.

Figure 13c discloses the temperature-dependent variation of the dissipation factor ($\tan\delta$) at various frequencies. The nearly constant variation $\tan(\delta)$ at low temperatures indicates restricted reorientation motion, achieving a loss asymmetric peak at 333 K. This later coincides with the temperature recorded by DSC at 321.5 K. Above this temperature, all curves decrease over the entire frequency range until stabilizing.

Figure 13d displays the frequency-dependent behavior of the real component of permittivity (ε') at different temperatures, characterized by an exponential decrease. Besides, it is to be noticed that the investigated sample exhibits higher (ε') values at low frequencies, reaching up to 10^3, suggesting its potential suitability for low-frequency energy storage applications. Improvements in energy storage capacity are shown by a drop in (ε') values with increasing frequency.[86] Literature indicates that our studied compound possesses a significantly higher dielectric constant compared to traditional inorganic semiconductors. For instance, silicon has a dielectric constant of 12.1,[87] while ferrite compounds typically exhibit dielectric constants ranging from 10^{-4} to 10.[88,89]

Furthermore, the reported Ni, Mn, and Sb-based hybrid materials have significant dielectric constants at lower frequencies, roughly within the range of $\varepsilon \sim 10^4$.[50,90,91] At higher frequencies, it exhibits low dielectric loss and strong electrical conductivity. Higher dielectric constants are associated with greater resistance to electric fields. Accordingly, the following Ge(II)-based compound could be a promising candidate for use in electronic devices, especially in the field of electronic capacitors.

4. CONCLUSIONS

The main objective of this study is to scrutinize the physical properties of a novel 0D Ge(II)-based hybrid perovskite with the formula $[NH_3(CH_2)_2NH_3]GeF_6$. The crystal structure consists of a periodic arrangement of organic groups as well as inorganic $[GeF_6]^{2-}$ octahedral, that are linked by N−H···F and C−H···F hydrogen bonds, forming a three-dimensional network. The thermal studies indicate the presence of one phase transition at 323 K, which is corroborated by electrical and dielectric analysis. The UV−vis absorption analysis revealed an optical band gap energy of 3.30 eV, confirming the semiconductor nature of the investigated material. This finding highlights its potential for optoelectronic applications. Besides, the photoluminescent properties revealed a broadband bluish light emission, generated from STEs of the inorganic octahedron, with a high CRI value. A deep investigation of the complex impedance across temperature and frequency ranges

https://doi.org/10.1021/acsomega.4c05255
ACS Omega 2024, 9, 42868−42882

enables the determination of the equivalent circuit, while the thermal evolution of this specific conductivity unveils its good semiconductor nature. Finally, the dielectric analysis suggests that the title compound exhibits a dielectric relaxation phenomenon, including higher dielectric permittivity. Based on these findings, we believe that the research work paves the way toward the design of novel halide-based perovskite materials that hold great promise as an alternative for electronic capacitor devices.

■ ASSOCIATED CONTENT

Supporting Information

The Supporting Information is available free of charge at https://pubs.acs.org/doi/10.1021/acsomega.4c05255.

Reagents used for the construction, crystal data and summary of intensity data collection and structure refinement, atomic coordinates and thermal agitation factors, Atomic displacement parameters, geometric characteristics of hydrogen bridge bonds and geometric parameters of the $[NH_3(CH_2)_2NH_3]GeF_6$ title compound (PDF)

Accession Codes

Supporting crystallographic data for this article in CIF format are available as an electronic supporting publication from Cambridge Crystallographic Data Centre (CCDC: **2149878**). This data can be obtained free of charge via https://www.ccdc.cam.ac.uk/community/deposita structure/CSD Communications/, or from the Cambridge Crystallographic Data Centre, 12 Union Road, Cambridge CB2 1EZ, U.K. (Fax: (international): + 441223/336033; email: deposit@ccdc.cam.ac.uk).

■ AUTHOR INFORMATION

Corresponding Author

Zakaria Elaoud − *Laboratory Physical-Chemistry of Solid-State, Faculty of Sciences, University of Sfax, 3000 Sfax, Tunisia*; Email: zakaria.elaoud@fss.usf.tn, Zakaria_elaoud@yahoo.com

Authors

Emna Ben Messaoud − *Laboratory Physical-Chemistry of Solid-State, Faculty of Sciences, University of Sfax, 3000 Sfax, Tunisia*; orcid.org/0009-0007-1247-1335

Dhouha Abid − *Laboratory Physical-Chemistry of Solid-State, Faculty of Sciences, University of Sfax, 3000 Sfax, Tunisia*; orcid.org/0000-0002-5967-5876

Slim Elleuch − *Laboratory of Applied Physics, Faculty of Sciences, University of Sfax, 3000 Sfax, Tunisia*

Abderrazek Oueslati − *Laboratory of Spectroscopic Characterization and Optical Materials, Faculty of Sciences, University of Sfax, 3000 Sfax, Tunisia*

Philippe Guionneau − *Univ. Bordeaux, CNRS, Bordeaux INP, ICMCB, UMR 5026, F-33600 Pessac, France*

Stanislav Pechev − *Univ. Bordeaux, CNRS, Bordeaux INP, ICMCB, UMR 5026, F-33600 Pessac, France*

Nathalie Daro − *Univ. Bordeaux, CNRS, Bordeaux INP, ICMCB, UMR 5026, F-33600 Pessac, France*

Complete contact information is available at: https://pubs.acs.org/10.1021/acsomega.4c05255

Author Contributions

All authors contributed to the discussions and revisions of the manuscript. E.B.M.: Characterization, writing, original draft, methodology, data curation, conceptualization. D.A.: Conceptualization, characterization, writing, validation. S.E.: Data curation, Investigation. A.O.: Original draft, data curation. P.G.: Validation, supervision. S.P.: Validation, supervision. N.D.: Validation, supervision. Z.E.: Supervision, review, methodology.

Notes

The authors declare no competing financial interest.

■ ACKNOWLEDGMENTS

A great thanks to ICMCB Bordeaux France, especially the XR diffraction service.

■ REFERENCES

(1) Shekhawat, V. Graphite-Paper Circuit Elements: Resistor, Capacitor, and π Value Estimation. *Phys. Teach.* **2023**, *61* (2), 154−155.

(2) Chung, D. D. L.; Xi, X. Introducing Solder-Based Electronics, with Solder Functioning as Resistor, Capacitor, and Power Source. *J. Mater. Sci.: Mater. Electron.* **2023**, *34* (2), No. 131.

(3) Bărbulescu, C.; Căiman, D.-V.; Nanu, S.; Dragomir, T.-L. Implementation of Parameter Observer for Capacitors. *Sensors* **2023**, *23* (2), No. 948.

(4) Saafan, E.; Saafan, E.; Lazimov, T. Technical and Physical Problems of Engineering, 2022. www.iotpe.com.

(5) Lim, S.-T.; Lee, K.-Y.; Chae, D.-J.; Lim, S.-H. Design of Mid-Point Ground with Resistors and Capacitors in Mono-Polar LVDC System. *Energies* **2022**, *15* (22), No. 8653.

(6) Banerjee, S.; Ghosh, M.; Mondal, P.; Ranjan, A. Third Order Inverse Multifunction Filter Employing Resistors and Capacitors. *Int. J. Numer. Modell.: Electron. Networks, Devices Fields* **2022**, *35* (5), No. e3002, DOI: 10.1002/jnm.3002.

(7) Schiavon, G. J.; Santos, O. R.; Batista, M. C.; Braga, W. S.; Bratti, V. M. Experimental Didactic Kit for Teaching Resistors, Capacitors and RC Timing Circuits. *Phys. Educ.* **2022**, *57* (5), No. 055019.

(8) Quadir, M. S. E.; Chandy, J. A. Integrated Circuit Authentication Based on Resistor and Capacitor Variations of a Low Pass Filter (LoPUF). *Int. J. High Speed Electron. Syst.* **2022**, *31*, No. 2240014, DOI: 10.1142/S0129156422400146.

(9) Rehman, M. U.; Manan, A.; Khan, M. A.; Uzair, M.; Qazi, I.; Iqbal, Y.; Ullah, A.; Ahmad, A. S. Improved Energy Storage Performance of $Bi(Mg_{0.5}Ti_{0.5})O_3$ Modified $Ba_{0.55}Sr_{0.45}TiO_3$ Lead-Free Ceramics for Pulsed Power Capacitors. *J. Eur. Ceram. Soc.* **2023**, *43* (6), 2426−2441.

(10) Shang, F.; Wei, J.; Xu, J.; Zhang, G.; Li, M.; Xu, K.; Liu, X.; Li, B.; Huang, H.; Chen, G.; Xu, H. Glass-Ceramic Capacitors with Simultaneously High Power and Energy Densities under Practical Charge−Discharge Conditions. *ACS Appl. Mater. Interfaces* **2022**, *14* (47), 53081−53089.

(11) Uhlenbruck, S. A Physical Derivation of the Capacitive Brick Layer Model in Polycrystalline Ceramics from Fundamental Electrodynamic Equations. *J. Electrochem. Soc.* **2022**, *169* (10), No. 106509.

(12) Rohilla, R.; Khasa, S.; Hooda, A. Structural and Impedance Spectroscopic Investigations of Eco-Friendly Alkali Phosphoborate Glass−Ceramics Containing Zirconium Ion. *Environ. Sci. Pollut. Res.* **2023**, *30* (44), 98609−98618.

(13) Pan, Y.; Han, Y.; Chen, Y.; Li, D.; Tian, Z.; Guo, L.; Wang, Y. Benzoic Acid-Modified 2D Ni-MOF for High-Performance Supercapacitors. *Electrochim. Acta* **2022**, *403*, No. 139679.

(14) Liu, Y.; Yao, Z.; Zhou, J.; Jin, L.; Wei, B.; He, X. Facile Synthesis of MOF-Derived Concave Cube Nanocomposite by Self-Templated toward Lightweight and Wideband Microwave Absorption. *Carbon* **2022**, *186*, 574−588.

(15) Halder, L.; Bera, A.; Maitra, A.; Si, S. K.; De, A.; Ojha, S.; Bera, S.; Khatua, B. B. Comparative Supercapacitive Analysis of 2-Methylimidazole Derived Cobalt Nickel Oxides ($CoNiO_2$ and

Co_2NiO_4) and Subsequent Fabrication of Asymmetric Supercapacitor Devices. *J. Energy Storage* **2022**, *52*, No. 104993.
(16) Abid, D.; Abid, H.; Maalej, W.; Hlil, E.; Guionneau, P.; Pechev, S.; Daro, N.; Elaoud, Z. A 1D Helical Eco-Friendly Mn(II) Halide Coordination Polymer: Luminescent Properties Involving Resonant Energy Transfer and Magnetic Characterization. *J. Lumin.* **2022**, *252*, No. 119251.
(17) Abid, D.; Dhouib, I.; Guionneau, P.; Pechev, S.; Chaabane, I.; Daro, N.; Elaoud, Z. Proton Conduction Study of a New Selenate-Based Hybrid Compound. *J. Alloys Compd.* **2020**, *824*, No. 153826.
(18) Yang, W. S.; Park, B.-W.; Jung, E. H.; Jeon, N. J.; Kim, Y. C.; Lee, D. U.; Shin, S. S.; Seo, J.; Kim, E. K.; Noh, J. H.; Seok, S. Il. Iodide Management in Formamidinium-Lead-Halide−Based Perovskite Layers for Efficient Solar Cells. *Science* **2017**, *356* (6345), 1376−1379.
(19) Sahoo, S.; Deka, N.; Boomishankar, R. Piezoelectric Energy Harvesting of a Bismuth Halide Perovskite Stabilised by Chiral Ammonium Cations. *CrystEngComm* **2022**, *24* (35), 6172−6177.
(20) Zhan, Y.; Cheng, Q.; Song, Y.; Li, M. Micro-Nano Structure Functionalized Perovskite Optoelectronics: From Structure Functionalities to Device Applications. *Adv. Funct. Mater.* **2022**, *32* (24), No. 2200385, DOI: 10.1002/adfm.202200385.
(21) Elleuch, S.; Lusson, A.; Pillet, S.; Boukheddaden, K.; Abid, Y. White Light Emission from a Zero-Dimensional Lead Chloride Hybrid Material. *ACS Photonics* **2020**, *7* (5), 1178−1187.
(22) Barkaoui, H.; Abid, H.; Yangui, A.; Triki, S.; Boukheddaden, K.; Abid, Y. Yellowish White-Light Emission Involving Resonant Energy Transfer in a New One-Dimensional Hybrid Material: $(C_9H_{10}N_2)$-$PbCl_4$. *J. Phys. Chem. C* **2018**, *122* (42), 24253−24261.
(23) Medhioub, O.; Samet, A.; Barkaoui, H.; Triki, S.; Abid, Y. Multiexcitonic Broad-Band Emission Enhanced by Resonant Energy Transfer in a New Two-Dimensional Organic−Inorganic Perovskite: $(C_3H_8N_6)PbCl_4$. *J. Phys. Chem. C* **2020**, *124* (37), 20359−20366.
(24) Trabelsie, S.; Samet, A.; Dammak, H.; Michaud, F.; Santos, L.; Abid, Y.; Chaabouni, S. Optical Properties of a New Luminescent Hybrid Material $[C_6N_2H_5]_3BiCl_6$ Involving a Resonance Energy Transfer (RET). *Opt. Mater.* **2019**, *89*, 355−360.
(25) Lee, A. Y.; Park, D. Y.; Jeong, M. S. Correlational Study of Halogen Tuning Effect in Hybrid Perovskite Single Crystals with Raman Scattering, X-Ray Diffraction, and Absorption Spectroscopy. *J. Alloys Compd.* **2018**, *738*, 239−245.
(26) Zhang, X.-M.; Li, P.; Gao, W.; Liu, J.-P. Spin-Canting Magnetization in 3D Metal Organic Frameworks Based on Strip-Shaped Δ-Chains. *RSC Adv.* **2015**, *5* (94), 76752−76758.
(27) Li, X.; Gao, X.; Zhang, X.; Shen, X.; Lu, M.; Wu, J.; Shi, Z.; Colvin, V. L.; Hu, J.; Bai, X.; Yu, W. W.; Zhang, Y. Lead-Free Halide Perovskites for Light Emission: Recent Advances and Perspectives. *Adv. Sci.* **2021**, *8* (4), No. 2003334, DOI: 10.1002/advs.202003334.
(28) Li, C.; Sun, H.; Gan, S.; Dou, D.; Li, L. Perovskite Single Crystals: Physical Properties and Optoelectronic Applications. *Mater. Futures* **2023**, *2* (4), No. 042101.
(29) Baikie, T.; Fang, Y.; Kadro, J. M.; Schreyer, M.; Wei, F.; Mhaisalkar, S. G.; Graetzel, M.; White, T. J. Synthesis and Crystal Chemistry of the Hybrid Perovskite $(CH_3NH_3)PbI_3$ for Solid-State Sensitised Solar Cell Applications. *J. Mater. Chem. A* **2013**, *1* (18), 5628−5641.
(30) Cheng, P.; Wu, T.; Zhang, J.; Li, Y.; Liu, J.; Jiang, L.; Mao, X.; Lu, R.-F.; Deng, W.-Q.; Han, K. $C_6H_5C_2H_4NH_3)_2$ GeI_4 : A Layered Two-Dimensional Perovskite with Potential for Photovoltaic Applications. *J. Phys. Chem. Lett.* **2017**, *8* (18), 4402−4406.
(31) Chouaib, H.; Karoui, S.; Kamoun, S. Thermal Analysis, AC Conductivity and Dielectric Relaxation in Bis(2-Methoxyanilinium) Hexabromidostannate(IV) Dihydrate: $(C_7H_{10}NO)_2SnBr_6{\cdot}2H_2O$. *J. Mater. Sci.: Mater. Electron.* **2017**, *28* (21), 15835−15845.
(32) Karoui, S.; Kamoun, S. Synthesis, Characterization, Electrostatic Molecular Potential, H-Bond Energy, Spectroscopic Properties and Phase Transitions of < β>NH3(CH2)2NH3SnCl6. *J. Mol. Struct.* **2021**, *1238*, No. 130456.
(33) Braiek, F.; Elleuch, S.; Marzouki, R.; Graia, M. Experimental and Theoretical Studies of the Structural, Vibrational and Optical Properties of a New Hybrid Material $(C_5H_6N_2Cl)_2SiF_6$. *J. Mol. Struct.* **2021**, *1232*, No. 129990.
(34) Elaoud, Z.; Chaabouni, S.; Daoud, A.; Kamoun, S. Chemical preparation and crystalline structure of ethylendiammonium hexafluorosilicate $NH_3(CH_2)_2NH_3SiF_6$. *C. R. Acad. Sci., Ser. II: Mec., Phys., Chim., Astron.* **1995**, *320*, 551−555.
(35) Ouasri, A.; Rhandour, A.; Saadi, M.; Ammari, L. El. X-Ray, Dsc, Tga-Dtga, and Vibrational Studies of the Propylenediammonium Hexafluorosilicate $NH_3(CH_2)_3NH_3SiF_6$. *Biointerface Res. Appl. Chem.* **2021**, *11* (5), 12618−12632.
(36) Ouasri, A.; Rhandour, A.; Saadi, M.; El Ammari, L. Butane-1,4-Diammonium Hexafluorosilicate. *Acta Crystallogr., Sect E: Struct. Rep. Online* **2014**, *70* (2), o174.
(37) Ouasri, A.; Elyoubi, M. S. D.; Rhandour, A.; Georgieva, I.; Zahariev, T.; Trendafilova, N.; Roussel, P. X-Ray Structures, Solid State Periodic DFT Modeling and Vibrational Study of Alkylenediammonium Hexachlorostannates Compounds $NH_3(CH_2)_nNH_3SnCl_6$ (n = 3, 4, 5). *J. Mol. Struct.* **2019**, *1177*, 55−67.
(38) Belfaquir, M.; Elyoubi, M. S.; Rhandour, A.; Roussel, P. Structure of Pentylenediammoniumhexachlorostannate(IV). *Mater. Today: Proc.* **2019**, *13*, 615−620.
(39) Abdel-Aal, S. K.; Ouasri, A. Structural, BFDH Morphology, DSC, Infrared, and UV Absorption Studies of Tetrachlorocobaltate and Manganate $NH_3(CH_2)_nNH_3MCl_4$ (M: Co, Mn, and n = 4, 5, 9) Hybrid Perovskite Salts. *Polyhedron* **2023**, *246*, No. 116700.
(40) Abdi, M.; Zouari, F.; Chaabouni, S.; Elaoud, Z.; Salah, A. B. Phase Transition in the Compound $NH_3(CH_2)_5$ NH_3TlCl_5. *Phase Transitions* **2003**, *76* (8), 723−731.
(41) Tahiri, O.; Kassou, S.; El Mrabet, R.; Belaaraj, A. Synthesis, Hirshfeld Surface Analysis, Optical and Electronic Properties of the Functional Hybrid Perovskite $[NH_3{-}(CH_2)_2{-}NH_3]$ $CdCl_4$: A Combined Experimental and Theoretical Study. *Mater. Res. Express* **2019**, *6* (7), No. 076301.
(42) Farrugia, L. J. WinGX and ORTEP for Windows: An Update. *J. Appl. Crystallogr.* **2012**, *45* (4), 849−854.
(43) Sheldrick, G. M. SHELXS86 Program for Crystal Structure solution. *Acta Crystallogr.* **1986**, *A24*, 351−359.
(44) Sheldrick, G. M. A Short History of SHELX. *Acta Crystallogr., Sect. A: Found. Crystallogr.* **2008**, *64* (1), 112−122.
(45) Brandenburg, K. *Diamond*, version 4, 0; Impact GbR: Bonn, Germany, 2009.
(46) Baur, W. H. The Geometry of Polyhedral Distortions. Predictive Relationships for the Phosphate Group. *Acta Crystallogr., Sect. B: Struct. Crystallogr. Cryst. Chem.* **1974**, *30* (5), 1195−1215.
(47) Souidi, H.; Triki, H.; Kamoun, S. Synthesis, Crystal Structure, High-Resolution $L^{13}Cd$ and ^{13}C MAS NMR Investigation and Dielectric Study of $[C_2H_{10}N_2]Cd$ $(SCN)_4$. *J. Mol. Struct.* **2021**, *1232*, No. 129994.
(48) Brown, I. D. On the Geometry of O−H···O Hydrogen Bonds. *Acta Crystallogr., Sect. A* **1976**, *32* (1), 24−31.
(49) Maalej, W.; Hajlaoui, F.; Karoui, K.; Audebrand, N.; Roisnel, T. Crystal Structure and Semiconductor Properties of Copper(II) Complex Incorporating Chiral (R)-(+)-α-Ethylbenzylammonium Cations:$[(R)\text{-}C_9H_{14}N]_3[CuBr_4]$.Br. *J. Solid State Chem.* **2022**, *305*, No. 122646.
(50) Abid, D.; Mjejri, I.; Oueslati, A.; Guionneau, P.; Pechev, S.; Daro, N.; Elaoud, Z. A Nickel-Based Semiconductor Hybrid Material with Significant Dielectric Constant for Electronic Capacitors. *ACS Omega* **2024**, *9* (11), 12743−12752, DOI: 10.1021/acsomega.3c08499.
(51) Khawla, M.; Dhouha, A.; Ikram, D.; Slim, E.; Ali, O.; Zakaria, E. A 0D Lead-Free Nickel Halide-Based Perovskite Exhibiting Greenish Light Emission and High Color Rendering Index. *Mater. Res. Bull.* **2023**, *167*, No. 112396.
(52) Tauc, J.; Menth, A. States in the Gap. *J. Non-Cryst. Solids* **1972**, *8−10*, 569−585.

https://doi.org/10.1021/acsomega.4c05255
ACS Omega 2024, 9, 42868−42882

(53) Stoumpos, C. C.; Frazer, L.; Clark, D. J.; Kim, Y. S.; Rhim, S. H.; Freeman, A. J.; Ketterson, J. B.; Jang, J. I.; Kanatzidis, M. G. Hybrid Germanium Iodide Perovskite Semiconductors: Active Lone Pairs, Structural Distortions, Direct and Indirect Energy Gaps, and Strong Nonlinear Optical Properties. *J. Am. Chem. Soc.* **2015**, *137* (21), 6804−6819.
(54) Rana, A.; Vashistha, N.; Kumar, A.; Kumar, M.; Singh, R. K. Charge Carrier Formation Following Energy Gap Law in Photo-Activated Organic Materials for Efficient Solar Cells. *Energies* **2024**, *17* (9), No. 2114.
(55) Sun, S.; Lu, M.; Gao, X.; Shi, Z.; Bai, X.; Yu, W. W.; Zhang, Y. 0D Perovskites: Unique Properties, Synthesis, and Their Applications. *Adv. Sci.* **2021**, *8* (24), No. 2102689, DOI: 10.1002/advs.202102689.
(56) Krimi, M.; Hajlaoui, F.; Abdelbaky, M. S. M.; Garcia-Granda, S.; Rhaiem, A. B. Investigation of Optical, Dielectric, and Conduction Mechanism in Lead-Free Perovskite $CsMnBr_3$. *RSC Adv.* **2024**, *14* (15), 10219−10228.
(57) Kaiser, C.; Sandberg, O. J.; Zarrabi, N.; Li, W.; Meredith, P.; Armin, A. A Universal Urbach Rule for Disordered Organic Semiconductors. *Nat. Commun.* **2021**, *12* (1), No. 3988.
(58) Kchaou, H.; Karoui, K.; Khirouni, K.; Rhaiem, A. B. Optical and Dielectric Relaxation of Transition Metal-Based Organic-Inorganic Hybrid Materials. *J. Alloys Compd.* **2017**, *728*, 936−943.
(59) Hu, S.; Lewis, N. S.; Ager, J. W.; Yang, J.; McKone, J. R.; Strandwitz, N. C. Thin-Film Materials for the Protection of Semiconducting Photoelectrodes in Solar-Fuel Generators. *J. Phys. Chem. C* **2015**, *119* (43), 24201−24228.
(60) Feddaoui, I.; Abdelbaky, M. S. M.; García-Granda, S.; Essalah, K.; Ben Nasr, C.; Mrad, M. L. Synthesis, Crystal Structure, Vibrational Spectroscopy, DFT, Optical Study and Thermal Analysis of a New Stannate(IV) Complex Based on 2-Ethyl-6-Methylanilinium $(C_9H_{14}N)_2[SnCl_6]$. *J. Mol. Struct.* **2019**, *1186*, 31−38.
(61) Huang, J.; Su, B.; Song, E.; Molokeev, M. S.; Xia, Z. Ultra-Broad-Band-Excitable Cu(I)-Based Organometallic Halide with Near-Unity Emission for Light-Emitting Diode Applications. *Chem. Mater.* **2021**, *33* (12), 4382−4389.
(62) Zhou, C.; Tian, Y.; Yuan, Z.; Lin, H.; Chen, B.; Clark, R.; Dilbeck, T.; Zhou, Y.; Hurley, J.; Neu, J.; Besara, T.; Siegrist, T.; Djurovich, P.; Ma, B. Highly Efficient Broadband Yellow Phosphor Based on Zero-Dimensional Tin Mixed-Halide Perovskite. *ACS Appl. Mater. Interfaces* **2017**, *9* (51), 44579−44583.
(63) Sayer, I.; Dege, N.; Ghalla, H.; Naïli, H. Low PH-Induced Lone-Pair Activity in the Hybrid $(C_6H_{10}N_2)[SnCl_3]Cl$: Chemical Study and Physical Characterizations. *J. Mol. Struct.* **2022**, *1248*, No. 131403.
(64) Smith, M. D.; Jaffe, A.; Dohner, E. R.; Lindenberg, A. M.; Karunadasa, H. I. Structural Origins of Broadband Emission from Layered Pb−Br Hybrid Perovskites. *Chem. Sci.* **2017**, *8* (6), 4497−4504.
(65) Zhou, C.; Lin, H.; Tian, Y.; Yuan, Z.; Clark, R.; Chen, B.; van de Burgt, L. J.; Wang, J. C.; Zhou, Y.; Hanson, K.; Meisner, Q. J.; Neu, J.; Besara, T.; Siegrist, T.; Lambers, E.; Djurovich, P.; Ma, B. Luminescent Zero-Dimensional Organic Metal Halide Hybrids with near-Unity Quantum Efficiency. *Chem. Sci.* **2018**, *9* (3), 586−593.
(66) Yuan, Z.; Zhou, C.; Tian, Y.; Shu, Y.; Messier, J.; Wang, J. C.; van de Burgt, L. J.; Kountouriotis, K.; Xin, Y.; Holt, E.; Schanze, K.; Clark, R.; Siegrist, T.; Ma, B. One-Dimensional Organic Lead Halide Perovskites with Efficient Bluish White-Light Emission. *Nat. Commun.* **2017**, *8* (1), No. 14051.
(67) Abbassi, M.; Ternane, R.; Sobrados, I.; Madani, A.; Trabelsi-Ayadi, M.; Sanz, J. Ionic Conductivity of Apatite-Type Solid Electrolyte Ceramics $Ca_{2-x}Ba_xLa_4Bi_4(SiO_4)6O_2$ $(0 \leq x \leq 2)$. *Ceram. Int.* **2013**, *39* (8), 9215−9221.
(68) Khalfa, M.; Oueslati, A.; Khirouni, K.; Gargouri, M.; Rousseau, A.; Lhoste, J.; Bardeau, J.-F.; Corbel, G. Synthesis, Structural and Electrical Characterization of a New Organic Inorganic Bromide: $[(C_3H_7)_4N]_2$ $CoBr_4$. *RSC Adv.* **2022**, *12* (5), 2798−2809.
(69) Nefzi, H.; Sediri, F.; Hamzaoui, H.; Gharbi, N. Electric Conductivity Analysis and Dielectric Relaxation Behavior of the Hybrid Polyvanadate $(H_3N(CH_2)_3NH_3)[V_4O1_0]$. *Mater. Res. Bull.* **2013**, *48* (5), 1978−1983.
(70) Kumar, A.; Singh, B. P.; Choudhary, R. N. P.; Thakur, A. K. Characterization of Electrical Properties of Pb-Modified BaSnO3 Using Impedance Spectroscopy. *Mater. Chem. Phys.* **2006**, *99* (1), 150−159.
(71) Kossi, S. E. L.; Rhouma, F. I. H.; Dhahri, J.; Khirouni, K. Structural and Electric Properties of $La_{0.7}Sr_{0.25}Na_{0.05}Mn_{0.9}Ti_{0.1}O_3$ Ceramics. *Phys. B* **2014**, *440*, 118−123.
(72) Ram, M. Synthesis and Electrical Properties of $(Li-Co_{3/5}Fe_{1/5}Mn_{1/5})$ VO_4 Ceramics. *Solid State Sci.* **2010**, *12* (3), 350−354.
(73) Nadeem, M.; Akhtar, M. J. Melting/Collapse of Charge Orbital Ordering and Spread of Relaxation Time with Frequency in $La_{0.50}Ca_{0.50}MnO_{3+\delta}$ by Impedance Spectroscopy. *J. Appl. Phys.* **2008**, *104* (10), No. 103713, DOI: 10.1063/1.3028264.
(74) Lanfredi, S. Electric Conductivity and Relaxation in Fluoride, Fluorophosphate and Phosphate Glasses: Analysis by Impedance Spectroscopy. *Solid State Ionics* **2002**, *146* (3−4), 329−339.
(75) Weslati, N.; Gzaiel, M. B.; Chaabane, I.; Hlel, F. Ionic Conduction Mechanism and Relaxation Studies of $NaNbAlP_3O_{12}$ Compound. *Ionics* **2018**, *24* (1), 181−188.
(76) Kulkarni, S.; Nagabhushana, B. M.; Parvatikar, N.; Koppalkar, A.; Shivakumara, C.; Damle, R. Dielectric and Electrical Studies of Pr^{3+} Doped Nano $CaSiO_3$ Perovskite Ceramics. *Mater. Res. Bull.* **2014**, *50*, 197−202.
(77) Howell, F. S.; Bose, R. A.; Macedo, P. B.; Moynihan, C. T. Electrical Relaxation in a Glass-Forming Molten Salt. *J. Phys. Chem. A* **1974**, *78* (6), 639−648.
(78) Bishop, A. R.; Campbell, D. K.; Lomdahl, P. S.; Horovitz, B.; Phillpot, S. R. Breathers and Photoinduced Absorption in Polyacetylene. *Phys. Rev. Lett.* **1984**, *52* (8), No. 671.
(79) Mahfoudh, N.; Karoui, K.; Jomni, F.; Rhaiem, A. B. Structural Phase Transition, Thermal Analysis, and Spectroscopic Studies in an Organic−Inorganic Hybrid Crystal: $[(CH_3)_2NH_2]_2$ $ZnBr_4$. *Appl. Organomet. Chem.* **2020**, *34* (7), No. e5656, DOI: 10.1002/aoc.5656.
(80) Chaabane, I.; Rekik, W.; Ghalla, H.; Zaghrioui, M.; Lhoste, J.; Oueslati, A. Crystal Structure, Optical Characterization, Conduction and Relaxation Mechanisms of a New Hybrid Compound $(C_6H_9N_2)_2$ $[Sb_2Cl_8]$. *RSC Adv.* **2024**, *14* (5), 3588−3598.
(81) Gordon, K. L.; Kang, J. H.; Park, C.; Lillehei, P. T.; Harrison, J. S. A Novel Negative Dielectric Constant Material Based on Phosphoric Acid Doped Poly(Benzimidazole). *J. Appl. Polym. Sci.* **2012**, *125* (4), 2977−2985.
(82) Hajlaoui, S.; Chaabane, I.; Oueslati, A.; Guidara, K. Anomalous Dielectric Behavior in Centrosymmetric Organic−Inorganic Hybrid Bis-Tetrapropylammonium Hexachlorostannate. Crystal Structure and Properties. *Solid State Sci.* **2013**, *25*, 134−142.
(83) Piecha, A.; Gągor, A.; Węcławik, M.; Jakubas, R.; Medycki, W. Anomalous Dielectric Behaviour in Centrosymmetric Organic−Inorganic Hybrid Chlorobismuthate(III) Containing Functional N,N-Dimethylethylammonium Ligand. Crystal Structure and Properties. *Mater. Res. Bull.* **2013**, *48* (1), 151−157.
(84) Mansour, S. A.; Yahia, I. S.; Yakuphanoglu, F. The Electrical Conductivity and Dielectric Properties of C.I. Basic Violet 10. *Dyes Pigm.* **2010**, *87* (2), 144−148.
(85) Hamdi, M.; Karoui, S.; Oueslati, A.; Kamoun, S.; Hlel, F. Synthesis, Crystal Structure and Dielectric Properties of the New Organic-Inorganic Hybrid Compound $[C_6H_{10}N_2]_7[Bi_2Cl_{11}]_{2.4}[Cl]$. *J. Mol. Struct.* **2018**, *1154*, 516−523.
(86) gzaiel, M. b.; Garoui, I.; Almutairi, F. N.; Mbarek, I.; A, O. Lead-Free Halide Perovskites for Optoelectronic Application: Investigation of Structural, Optical, Electric and Dielectric Behaviors. *Opt. Mater.* **2024**, *154*, No. 115664.
(87) Armin, A.; Stoltzfus, D. M.; Donaghey, J. E.; Clulow, A. J.; Nagiri, R. C. R.; Burn, P. L.; Gentle, I. R.; Meredith, P. Engineering Dielectric Constants in Organic Semiconductors. *J. Mater. Chem. C* **2017**, *5* (15), 3736−3747.

https://doi.org/10.1021/acsomega.4c05255
ACS Omega 2024, 9, 42868−42882

(88) Hcini, D.; Hcini, S.; Charguia, R.; Maatallah, T.; Jabli, F.; Dhahri, A.; Khirouni, K.; Bouazizi, M. L. Effects of Varying Calcination Temperatures on the Optoelectronic and Electrical Properties of $Ni_{0.4}Cu_{0.4}Cd_{0.2}FeCrO_4$ Spinel Ferrites. *J. Mater. Sci.: Mater. Electron.* **2024**, *35* (16), No. 1062.
(89) Slima, I. B.; Karoui, K.; Mahmoud, A.; Boschini, F.; Rhaiem, A. B. Structural, Optical, Electric and Dielectric Characterization of a NaCu 0.2 Fe 0.3 Mn 0.5 O 2 Compound. *RSC Adv.* **2022**, *12* (3), 1563−1570.
(90) Gzaiel, M. B.; Oueslati, A.; Hlel, F.; Gargouri, M. Synthesis, Crystal Structure, Phase Transition and Electrical Conduction Mechanism of the New $[(C_3H_7)_4N]_2$ $MnCl_4$ Compound. *Phys. E* **2016**, *83*, 405−413.
(91) Weslati, N.; Chaabane, I.; Bulou, A.; Hlel, F. Synthesis, Crystal Structure, Thermal and Dielectric Properties of Tetrapropylammonium Tetrachloroantimonate(III). *Phys. B* **2014**, *441*, 42−46.

https://doi.org/10.1021/acsomega.4c05255
ACS Omega 2024, 9, 42868−42882